Structural, vibrational and magnetic properties of monoclinic La$_2$FeMnO$_6$ double perovskite

Raí F. Jucá [a], Gilberto D. Saraiva [b,*], A.J. Ramiro de Castro [c], Francisco F.de Sousa [d], Francisco G.S. Oliveira [e], Igor F. Vasconcelos [e], G.D.S. Souza [d], João M. Soares [f], Carlos H.N. Cordeiro [g], W. Paraguassu [d]

[a] Departamento de Física, Universidade Federal de Sergipe, São Cristóvão, 49100-000, Sergipe, Brazil
[b] Faculdade de Educação Ciências e Letras do Sertão Central, Universidade Estadual do Ceará, Quixadá, CE, 63902-098, Brazil
[c] Universidade Federal do Ceará, 63902-580, Quixadá, CE, Brazil
[d] Instituto de Ciências Exatas e Naturais, Universidade Federal do Pará, CEP, 66075-110, Belém, PA, Brazil
[e] Pós-graduação em Engenharia e Ciências de Materiais, Centro de Tecnologia, Universidade Federal do Ceara, Campus do Pici, Bloco 729, 60440-900, Fortaleza, CE, Brazil
[f] Departamento de Física, Universidade do Estado do Rio Grande do Norte, Mossoró-RN, CEP, 59610-210, Brazil
[g] Departamento de Física, Universidade Federal do Ceará, Caixa Postal 6030, Campus do Pici, CEP, 60455-970, Fortaleza, Ceará, Brazil

ARTICLE INFO

ABSTRACT

We report the synthesis of the double perovskite La$_2$FeMnO$_6$ and a complete characterization of this system by using X-ray diffraction, Raman and Fourier transform infrared (FT-IR) spectroscopy, scanning electron microscopy (SEM), vibrating sample magnetometer, Mossbauer spectroscopy and lattice dynamic calculations. The ambient structure of the La$_2$FeMnO$_6$ was well refined using monoclinic system and $P2_1/n$-space group, with two formulas per unit cell (Z = 2). SEM reveals that the sample is formed by particles with quasi-spherical morphology, randomly distributed in clusters. The investigation by Mössbauer spectroscopy identified that the incorporation of iron atoms occurred successfully in the analyzed structure since two paramagnetic phases were identified. The magnetization versus applied field (MxH) curve of La$_2$FeMnO$_6$ at room temperature is discussed. The LFMO double perovskite EPR spectrum indicates the coexistence of paramagnetic resonance (PM) and antiferromagnetic resonance (AFM), being a strong indication of the coexistence of PM and AFM clusters. Moreover, vibrational properties were calculated using a rigid ion model in order to assign the experimental Raman and infrared bands. All these results making the La$_2$FeMnO$_6$ an interesting material with practical applications and for the scientific investigations.

1. Introduction

In general, double perovskites have a chemical formula A$_2$BMO$_6$, where A represents a chemical element of the family of alkaline metals, rare earth or lanthanides. The B and M are transition metals that are surrounded by oxygen bonds, thus forming two octahedral subnetworks BO$_6$ and MO$_6$. Specifically, these transition metals play an important role in the magnetic, vibrational, electrical and optical properties of the system [1–4]. Furthermore, double perovskite oxides are widely studied due to their important physical properties, for instance: high dielectric constant [1,2], magnetic [5–7],superconductivity [3,8–12], ferroelectricity [4,13,14], multiferroicity [15–17], electric polarization [12,

18–26] and colossal magnetoresistance [27,28]. Therefore, double perovskites are of extreme technological importance due to their applications in magnetoresistive devices operating at room temperature [29, 30], magnetic recording media [31], spintronic devices (such as magnetodielectric capacitors and spin filtering tunnel junctions) [32–36], photodetectors [37], LED [38–40], optical thermometers [41], photovoltaic cells [42–44], catalytic [45,46], photocatalytic [47,48], supercapacitors [49], microwave technology [50–52] and transistors [53]. Particularly, the semi-metallic La$_2$FeMnO$_6$ (LFMO) has stood out for being a promising candidate for technological devices.

The double perovskite La$_2$FeMnO$_6$ is a compound formed by the intertwining of LaFeO$_3$ and LaMnO$_3$ subnets, with Fe and Mn ions

---

sharing disordered sites. The La^{2+} cation is located in the interstitial region between the FeO_6 and MnO_6 octahedra. These octahedra are connected by the vertices alternating their position along the three directions. In addition, it has been reported in the literature that the double perovskite LFMO crystallizes in different crystalline structures, which will depend on the synthesis methods used [54–57]. Palakkal et al., produced the LFMO by the Pechini method, obtaining an orthorhombic structure [56]. When LFMO is synthesized using the ionic coordination reaction method, the system crystallizes in monoclinic structure with $P2_1/n$-space group [57]. The solid state [55] and sol-gel [54] reaction method produced LFMO with cubic structure belonging to Pm-3m space group. Furthermore, the LFMO compound present different types of magnetic ordering, depending on the different sample preparation processes [57–59]. The magnetic ordering of the LFMO double perovskite is based on the exchange interactions between the Fe^{+3}/Mn^{+3} transition metal ions that help to form ferromagnetic clusters (FM) [57,58]. Thus, the presence of metallic/rare earth ions of La^{2+}, Fe^{3+} and Mn^{3+} makes the structure of the LFMO more stable and its complex magnetic ordering more interesting.

The vibrational properties using the Raman spectroscopy technique on ordered A_2BMO_6 double perovskite oxides have been widely explored by the scientific community [60,61]. Particularly, the vibrational properties of the of La_2FeMnO_6 double perovskite, under ambient temperature conditions, were recently described by Dhilip et al., using the Raman technique [6,55]. The authors studied pure LFMO samples, crystallized in cubic phase with *Pm-3m*-space group, with lattice parameters $a = b = c = 3.912$ Å. Therefore, this work aims to investigate the structural, morphological, magnetic and vibrational properties of the La_2FeMnO_6 double perovskite crystallized in the monoclinic phase with $P2_1/n$-space group under ambient conditions. The lattice dynamic (LD) calculations were used to discuss the attributions of vibrational modes, in the monoclinic phase, and shed light on the transformation mechanisms of the La_2FeMnO_6 double perovskite.

2. Experimental procedure

2.1. Synthesis of La_2FeMnO_6

The polycrystalline samples of the double perovskite (La_2FeMnO_6) were synthesized through the technique of solid-state reaction, which basically consists of homogenization of the powder precursor samples. The starting powders were manually homogenized for 30 min using a mortar and pestle. Then, the mixture was subjected to heat treatment at a temperature of 1200 °C for 36 h in ambient atmosphere using a resistance muffle furnace (EDG) with a constant heating rate of 10 °C/ min. The LMFO sample was synthesized in a molar ratio of 1: 1: ½, for the following compounds, respectively: lanthanum (III) oxide (99.99%), manganese (II) oxide (99.99%) and oxide of iron (III) (99.99%) obtained from Sigma-Aldrich. The synthesized sample was cooled down to room temperature by the thermal inertia of the assembly (furnace, crucible and sample).

2.2. Characterization methods

The sample characterization was carried out through X-ray diffraction (XRD) and the data was acquired using a Rigaku XRD (Miniflex II) with Cu-K$_\alpha$ radiation of 1.5406 Å. The recording data was collected with step of 0.02 and scan rate of 2°/min, at room temperature. The Rietveld method was used to refine the XRD pattern using the EXPO2014 program to determine the structural parameters of the sample. Morphological analyses were performed using a high-resolution Scanning Electron Microscope, Mira3 LMU model from TESCAN, with EDS energy dispersive spectrometer coupled, Oxford model X-ACT with secondary electron beams and electron acceleration voltage of 10 kV. The magnetization (M) versus applied magnetic field (H) plots were obtained at room temperature using vibrating sample magnetometer (VSM,

homemade). VSM was calibrated using a standard reference (powder high purity nickel), supplied with the instrument. These data have been analyzed to obtain the saturation magnetization (Ms) and coercive field (Hc) for LFMO sample in powder form. The Mössbauer spectrum was obtained in a SEE Co model W302 Spectrometer at room temperature, in transmission mode, using a ^{57}Co radioactive source diffused in a rhodium matrix. Furthermore, the hyperfine parameters were evaluated using the NORMOS software package. The Raman spectrum was acquired in backscattering geometry by using a Jobin Yvon T64000 triple-grating spectrometer in subtractive mode, and with the slits set for a resolution of 2 cm^{-1}. A laser line with a wavelength of 514.5 nm of an Argon ion laser was used as the excitation source. The laser spot was focused through an Olympus microscope lens, with a focal distance of f = 20.5 mm and a numeric aperture of $NA = 0.35$. The Fourier-transform infrared (FT-IR) measurements were performed using a Bruker spectrometer equipment (Bruker, Rheinstetten, Germany) between 100 and 1100 cm^{-1}. The system belongs to a model Vertex 70, equipped with an accessory-setting A225/Q Platinum attenuated total reflectance (ATR) technique, and with a detector-setting RT-Dla TGS wide-range MIR-FTIR. The width aperture of 6 mm was used, allowing measurements of up to 100 cm^{-1} with a spectral resolution of about 4 cm^{-1} for 120 scans. The electron paramagnetic resonance spectrum (EPR) was measured at room temperature using a Bruker instrument, model EMXmicro.

3. Results and discussion

3.1. X-ray diffraction and morphology analyses

Fig. 1 shows the powder XRD pattern that was refined through the Rietveld method using EXPO2014 software to determine the structural parameters. The crystallographic data of the La_2FeMnO_6 was refined using the crystallographic data based on the La_2MnCoO_6 (ICSD – 4514503), in order to identify the position of the atoms of the unit cell, which has been characterized as a double perovskite [62,63]. The Rietveld refinement results show that LFMO structure has two intensity peaks characteristic of the planes (112) and (200), bellow 2θ = 80°, see Fig. 1. The structure of the LFMO double perovskite was identified as being monoclinic belonging to $P2_1/n$ space group, with two formulas per unit cell (Z = 2). The lattice parameters $a = 5.557$, $b = 5.562$, and $c = 7.873$ Å and atomic position parameters, can be seen on Table 1 and Table 2, respectively. According to our results obtained through the
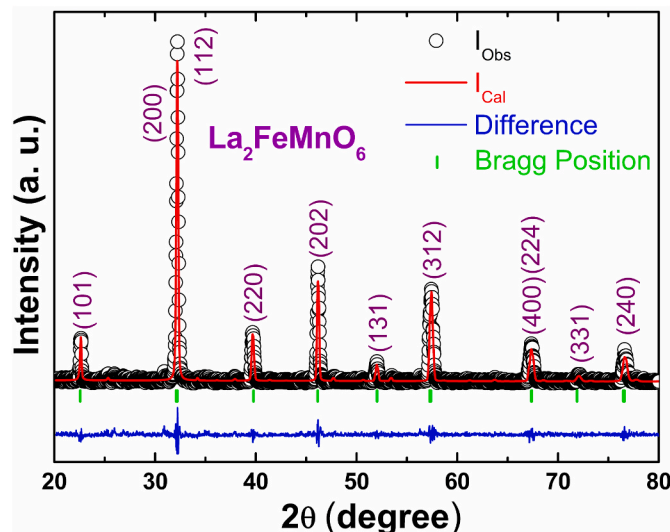

Fig. 1. Rietveld refinement of the XRD data for double perovskite La_2FeMnO_6, numbers in parenthesis are the Miller indices of the planes. The white circles and red lines represent the experimental pattern and its refinement, respectively.

Table 1
Rietveld refinement parameters and atomic coordinates of the double perovskite La$_2$FeMnO$_6$ monoclinic.

Empirical Formula	La$_2$FeMnO$_6$	La$_2$CoMnO$_6$
Crystal system	Refinement Monoclinic	Teoretical Monoclinic
Space Group	P2$_1$/n	P2$_1$/n
	Z = 2	Z = 2
Lattice Parameters (Å)	a = 5.557, b = 5.562 and c = 7.873 α = γ = 90.00° and β = 90.278°	a = 5.508, b = 5.436 and c = 7.736 α = γ = 90.00° and β = 90.05°
Volume (Å^3)	243.390	231.698
Rietveld Parameters:	R$_p$ = 21.267, R$_{wp}$ = 32.249, R$_{exp}$ = 29.391 and χ^2 = 1.204.	Reference: [62]

Rietveld refinement method, by using EXPO software, the value found for the average crystallite size of LFMO is approximately D$_{LFMO}$ = 2.65 μm. It is worthwhile mention that the LFMO double perovskite can crystalize in different phases, at room temperature, such as ortho-rhombic [58,64], cubic [55], and monoclinic [57], depending on the synthesis method used.

Fig. 2 shows the micrographs of the synthesized compound obtained by using SEM technique. The SEM micrographs reveal that the sample is formed by particles with quasi-spherical morphology, randomly distributed in clusters. The estimated average diameter obtained in the micrograph images through SEM was at around 2.375 μm, which is consistent with the average crystallite size obtained through Rietveld refinement, estimated at about 2.65 μm.

3.2. Vibrational properties under ambient conditions

The structure of the La$_2$FeMnO$_6$ at room-temperature belongs to the monoclinic phase (*P2$_1$/n*-space group), with two formula units per unit cell. The group theory analysis predicts a total of 60 vibrational modes at the centre of the Brillouin zone (**k** = 0), with 57 optical and three acoustic modes. The distribution of optical (Γ$_{optical}$) and acoustic (Γ$_{acoustic}$) modes according to the irreducible representations of the C$_{2h}$-factor group are, respectively, Γ$_{optical}$ = 12A$_g$ +12B$_g$ + 17A$_u$ + 16B$_u$ and Γ$_{acoustic}$ = A$_u$ + 2B$_u$. Fig. 3 shows the experimental Raman spectrum of the LFMO double perovskite at room temperature ranging from 80 to 850 cm^{-1} (bottom) and the inset of this figure shows the unit cells of La$_2$FeMnO$_6$ (top) in the monoclinic phase (*P2$_1$/n*-space group). Fig. 4 shows the experimental infrared spectrum of the LFMO double perovskite at room temperature ranging from 130 to 1100 cm^{-1}.

Based on our lattice dynamic (LD) calculations, the vibration wavenumbers of the observed and calculated Raman-active and IR-active modes with their assignments are list on Table 3 and Table 4, respectively.

In order to predict the assignment of Raman modes of LFMO double perovskite was used the LD calculation to predict the auto values and atomic displacement of the La$_2$FeMnO$_6$ compound. This LD is based on a

set of ionic potential, which is based on a model that treats the material as a collection of core systems, interacting in each other through short-range classic potentials. This model was successfully used for a number of molybdates and tungstates [65–68]. The interaction force constants were derived using the following relation:

$$f_{ij} = -\frac{1}{r}\frac{\partial U_{ij}(r)}{\partial r} \tag{1}$$

where f_{ij} and U_{ij} are the force constant and the related potential of interaction among the species i and j, and r is the distance between the interacting species. For the O–O interactions we have used the $U_{ij}(r)$ Buckingham potential reported previously [68].

For the interactions among Fe–O and Mn–O first neighborhood we have considered the partially covalent model, represent by a liner interatomic forces of the form

$$f_{ij}(r) = f_2 - f_3\,r \tag{2}$$

That refer to the anharmonic potential of the following form:

$$U_{ij}(r) = f_0 + f_2\frac{r^2}{2} - f_3\frac{r^3}{3} \tag{3}$$

where the f_2 and the f_3 are constants to be refined by a fitting of the experimental data. The lattice parameters and atomic positions for the La$_2$FeMnO$_6$, used as input parameters, were taken from Ref. [62]. The set of forces was obtained through the use of starting parameters in the phonon calculations performed with a Wilson's FG matrix method and a software package of VIBRATZ developed by Dowty [65]. The refinement of the force constants was performed to obtain the best fit the experimental data and the final force constants (in mDyn/Å) are shown on Table 5, which refer to the B–O bond of first neighborhood of each species (B = La, Fe, Mn and O). The calculated wavenumbers, together with the assignment of vibration modes, are listed on Table 3 and on Table 4, and some representative atomic displacements are presented in Fig. 5 and Fig. 6.

3.2.1. Ag Raman modes

Based on LD calculations, the Raman band centered at about 681.4 cm^{-1} (A$_g$) is attributed to a symmetric stretching (ν_1) of the octahedrons. Since each octahedron are bonded by eight octahedrons sharing the edge oxygen atom, it means that when oxygen atoms are moving away from one octahedron, they are approaching to the other along the chemical bond Mn–O–Fe. In another word, when one octahedron is expanding, the other is compressing and vice versa, see Fig. 5. The Raman modes centered at 647.5 cm^{-1} (A$_g$) (Fig. 5) and at 638.2 cm^{-1} (A$_g$) were assigned as asymmetric stretching (ν_3) of the octahedrons. The mode located at 567.9 cm^{-1} (A$_g$) was assigned to an in-plane scissoring of the octahedrons in the plane "bc" and the mode 488.3 cm^{-1} (A$_g$) was assigned to a bending mode, with a strong vibration of the oxygen atoms, with a large motion perpendicular to the Mn–O–Fe bond along of the diagonal of the unit cell. The mode centered at 471.6 cm^{-1} (A$_g$) was assigned as a bending mode with a strong vibration of the oxygen atoms
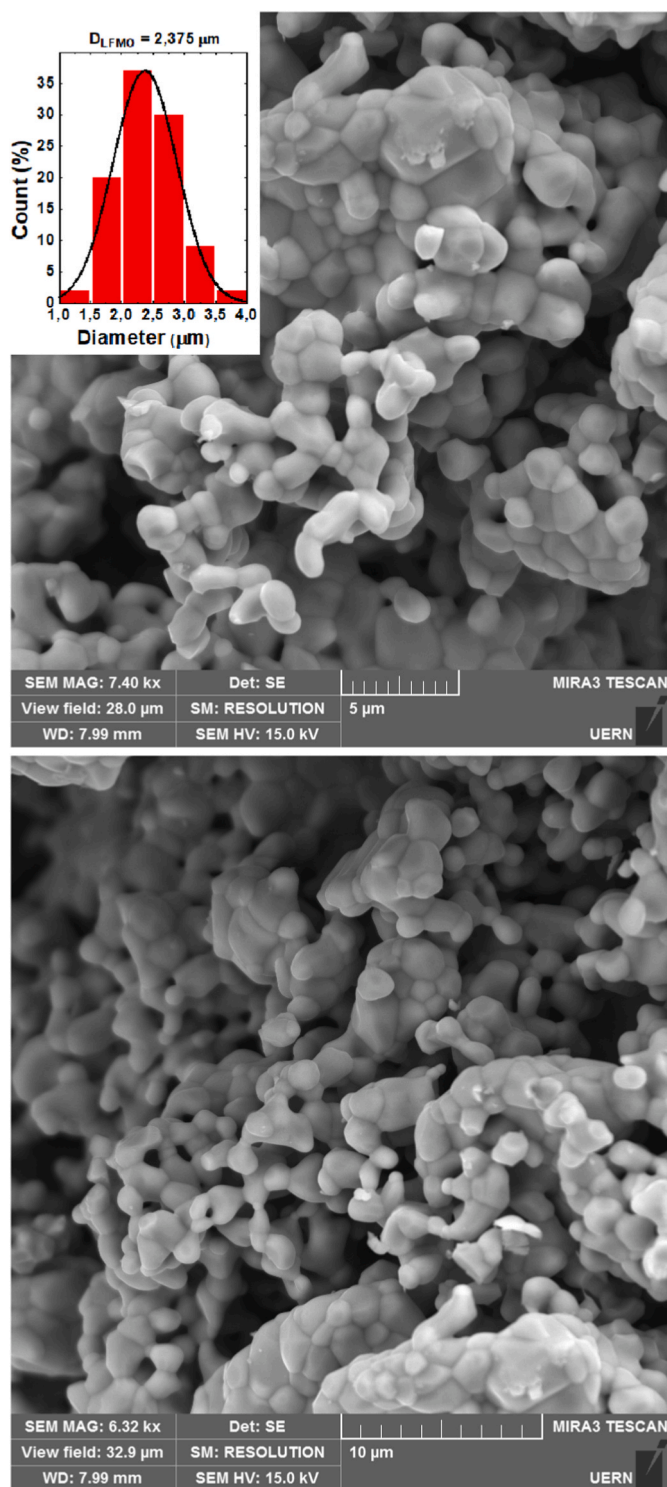
Table 2
Atoms and atomic position parameters.

Atoms	Ion	x	y	z	Occ.	Multiplicity	Wyckoff letter	Site symmetry
La1	La^{2+}	−0.0040	−0.0168	0.2530	1.000	4	e	1
Fe1	Fe^{3+}	0.0000	0.5000	0.5000	0.900	2	c	$\bar{1}$
Fe2	Fe^{3+}	0.5000	0.0000	0.0000	0.100	2	d	$\bar{1}$
Mn1	Mn^{3+}	0.0000	0.5000	0.2362	0.100	2	c	$\bar{1}$
Mn2	Mn^{3+}	0.5000	0.0000	0.0000	0.900	2	d	$\bar{1}$
O1	O^{2-}	0.2600	0.2500	0.0300	1.000	4	e	1
O2	O^{2-}	0.2100	0.2100	0.4780	1.000	4	e	1
O3	O^{2-}	0.5300	0.0030	0.2500	1.000	4	e	1

Fig. 2. Scanning electron micrographs at two magnifications of the double perovskite La_2FeMnO_6 and size distribution histogram.

Fig. 3. Experimental Raman spectrum of the double perovskite La_2FeMnO_6 at room temperature ranging from 80 cm^{-1}–850 cm^{-1} (bottom). Inset: Unit cells of La_2FeMnO_6 (top) in the monoclinic phase ($P2_1/n$-group space) (top).

Fig. 4. Experimental IR spectrum of the LFMO double perovskite at room temperature ranging from 130 cm^{-1}–1100 cm^{-1}.

perpendicular to the Mn–O–Fe along of the "bc" plane, while the mode at 468.1 cm^{-1} (A_g) was assigned as out-of-plane twisting of the octahedrons, with motion from the oxygen atoms along of the "b" axis. The mode at 431.2 cm^{-1} (A_g) was assigned to an in-plane rocking of the octahedrons with motions of the oxygen atoms in the "bc" plane (Fig. 5). The mode located at 359.8 cm^{-1} (A_g) was assigned to an out-of-plane twisting of the octahedrons with motion from the oxygen atoms perpendicular to the Mn–O–Fe bond along of the diagonal of the unit
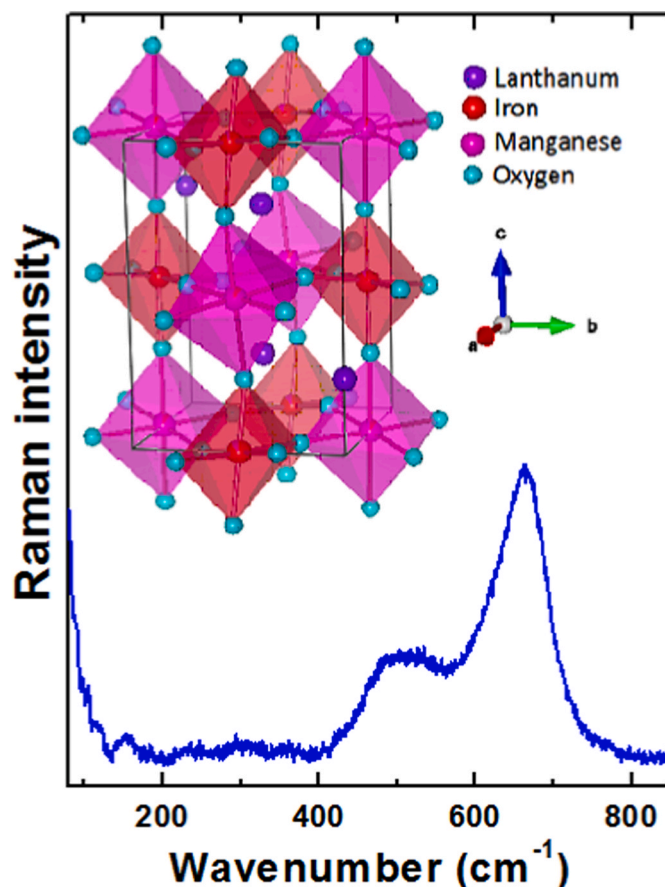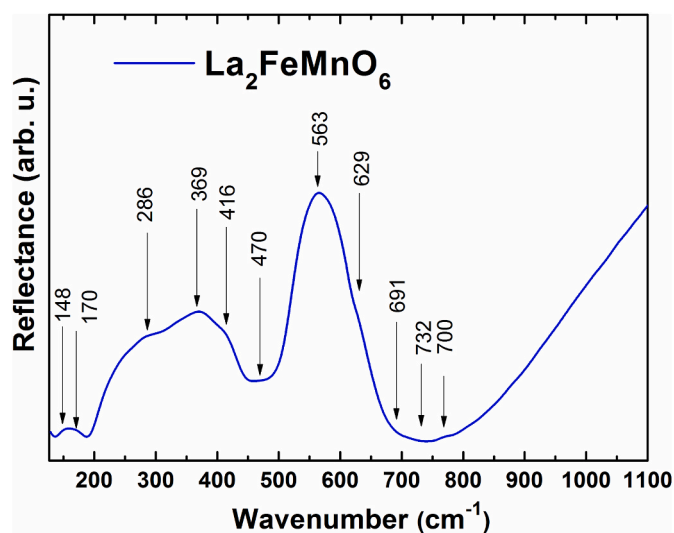
cell. The mode centered at 130.8 cm^{-1} (A_g) was assigned to a translational mode of the La atoms along of the "b" axis plus a bending of the octahedron with a strong vibration from the oxygen atoms along of the "b" axis (Fig. 5). The mode at 84.3 cm^{-1} (Ag) was assigned to a translational mode of the La atoms along of the plane "bc" plus a scissoring mode of the octahedron. The mode at 80.1 cm^{-1} (A_g) is assigned to a

Table 3

Observed and calculated Raman modes for the double perovskite La$_2$FeMnO$_6$ together with their assignments based on the lattice dynamic calculations for the monoclinic phase.

Raman ω_{obs}	Raman ω_{cal}	(Sym)	Assignments
697.41	681.4	A$_g$	Symmetric stretching mode (ν_1) of the octahedrons
680.58	667.3	B$_g$	Symmetric stretching mode ($\nu_1 + \nu_3$) of the octahedrons
660.86	661.4	B$_g$	Symmetric stretching mode ($\nu_1 + \nu_3$) of the octahedrons with a large motion of the oxygen atoms along of the "c" axis.
635.12	647.5	A$_g$	Asymmetric stretching mode (ν_3) of the octahedrons
612.75	639.0	B$_g$	Asymmetric stretching mode (ν_3) of the octahedrons with a large motion of the oxygen atoms along of the "ab" plane
	638.2	A$_g$	Asymmetric stretching mode (ν_3) of the octahedrons
583.88	567.9	A$_g$	Scissoring of the octahedrons with a large motion of the one oxygen atom in the plane "bc"
554.90	555.2	B$_g$	Wagging mode the octahedrons with a large motion of the oxygen atoms along of the "bc" plane
352.22	488.3	A$_g$	Bending mode with a strong vibration of the oxygen atoms perpendicular to the Mn–O–Fe bond along of the diagonal of the unit cell.
	487.0	B$_g$	Scissoring mode of the octahedrons in the plane "ab"
508.89	472.4	B$_g$	Twisting mode the octahedrons with motion of the oxygen atoms along of the axis "a"
	471.6	A$_g$	Bending mode with a strong vibration of the oxygen atoms perpendicular to the Mn–O–Fe along of the "bc" plane.
488.66	468.1	A$_g$	Twisting mode of the octahedrons with a large motion of some oxygen atoms along of the axis "b"
474.76	443.2	B$_g$	Bending mode mode the octahedrons
	438.8	B$_g$	Bending mode mode the octahedrons
460.32	431.2	A$_g$	Rocking mode of the octahedrons with motion of the oxygen atoms in the plane "bc"
364.78	361.9	B$_g$	Twisting mode of the octahedrons
	359.8	A$_g$	Twisting mode of the octahedrons with motion of the oxygen atoms perpendicular to the Mn–O–Fe bond along of the diagonal of the unit cell.
235	198.9	B$_g$	Translational mode of the La atoms a long of the "c" axis plus a twisting of the octahedron
1162.42	130.8	A$_g$	Translational mode of the La atom along of the "b" axis plus a bending of the octahedron with a strong vibration of the oxygen atoms along of the "b" axis.
1145.32	120	B$_g$	Translational mode of the La atoms a long of the "ab" plane plus a twisting of the octahedron
115	84.3	A$_g$	Translational mode of the La atom along of the "bc" axis plus a scissoring mode of the octahedrons.
104	80.1	A$_g$	Translational mode of the La atom along of the "ac" plane plus a twisting mode of the octahedrons in the plane "ac"
88	77.4	B$_g$	Translational mode of the La atoms a long of the "b" axis plus a wagging mode of the octahedrons

Table 4

Observed and calculated infrared modes for the double perovskite La$_2$FeMnO$_6$ together with their assignments based on the lattice dynamic calculations for the monoclinic phase.

IR ω_{obs}	IR ω_{cal}	(Sym)	Assignments
770	740.1	A$_u$	Asymmetric stretching mode (ν_3) of the octahedrons with large motion of the oxygen atoms along of the "c" axis and in the diagonal of the plane "ab"
	737.5	B$_u$	Asymmetric stretching mode (ν_3) of the octahedrons with large motion of the oxygen atoms along of the "c" axis and in the diagonal of the plane "ab"
732	733.4	B$_u$	Asymmetric stretching mode (ν_3) of the octahedrons with large motion of the oxygen atoms along of the "c" axis and in the diagonal of the plane "ab"
691	729.9	A$_u$	Asymmetric stretching mode (ν_3) of the octahedrons with the motion of the large motion of the oxygen atoms along of the "c" axis and in the diagonal of the plane "ab"
629	722.9	B$_u$	Asymmetric stretching mode (ν_3) of the octahedrons with large motion of the oxygen atoms along of the diagonal of the plane "ab"
	722.5	A$_u$	Asymmetric stretching mode (ν_3) of the octahedrons with a large motion of the oxygen atoms along of the "ab" plane
563	564.0	B$_u$	Wagging mode the octahedrons with a large motion oxygen atoms along of the diagonal of the unit cell.
	550.2	A$_u$	Wagging mode the octahedrons with a large motion of the oxygen atoms along of the diagonal of the unit cell.
	483.1	B$_u$	Wagging mode the octahedrons with a large motion oxygen atoms along of the "a" axis diagonal of the unit cell.
470	477.1	A$_u$	Wagging mode the octahedrons with the motion oxygen atoms along of the diagonal of the unit cell.
	474.1	A$_u$	Wagging mode the octahedrons with a large motion of the oxygen atoms along of the axis "a"
	468.2	B$_u$	Wagging mode the octahedrons with a large motion of the oxygen atoms along of the axis "b"
	464.7	B$_u$	Bending mode the octahedrons
	450.2	A$_u$	Wagging mode the octahedrons with a large motion of the oxygen atoms along of the diagonal of the "ac" plane
416	450.5	B$_u$	Wagging mode the octahedrons
	445.5	A$_u$	Wagging mode the octahedrons with a large motion of the oxygen atoms along of the diagonal of the "ab" plane
	397.5	A$_g$	Wagging mode the octahedrons with a large motion of the oxygen atoms along of the diagonal of the unit cell.
369	395.4	B$_u$	Wagging mode the octahedrons with a large motion of the oxygen atoms along of the diagonal of the "ac" plane
	335.8	A$_u$	Wagging mode the octahedrons with a motion of the oxygen atoms along of the diagonal of the unit cell
	330.4	B$_u$	Wagging mode the octahedrons
	323.3	B$_u$	Wagging mode the octahedrons
	315.3	A$_u$	Wagging mode the octahedrons with the motion of the oxygen atoms along of the diagonal of the unit cell
286	291.0	A$_u$	Wagging mode the octahedrons with a large motion of the oxygen atoms along of the diagonal of the unit cell.
	284.2	B$_u$	Wagging mode the octahedrons with the motion of the oxygen atoms along of the diagonal of the unit cell
170	186.8	A$_u$	Translational mode of the La atoms a long of the "c" axis plus a translational of the octahedron in the "ac" plane
148	133.7	B$_u$	Translational mode of the La atoms a long of the "c" axis plus a wagging of the octahedron with a large motion of the oxygen atoms a long of the "c" axis
	120.2	A$_u$	Translational mode of the La atoms a long of the diagonal of "ac" plane axis plus a wagging of the octahedrons.
	98.0	B$_u$	Translational mode of the La atoms a long of the "a" axis plus a wagging of the octahedron.
	95.0	A$_u$	Translational mode of the La atoms and the octahedron along of the axis "b"
	92.7	B$_u$	Translational mode of the La atoms a long of the "c" axis plus a wagging of the octahedron with a large motion of the oxygen atoms a long of the "c" axis

translational mode of the La atom along of the "ac" plane plus a twisting mode of the octahedrons in the plane "ac".

3.2.2. Bg Raman modes

The Raman modes centered at 667.3 cm^{-1} (B$_g$) (Figs. 5) and 661.4 cm^{-1} (B$_g$) were assigned to a combination of symmetric stretching (ν_1) plus an asymmetric stretching (ν_3) of the octahedrons, while the mode centered at 639.0 cm^{-1} (B$_g$) was assigned to an asymmetric stretching (ν_3) of the octahedrons (Fig. 5). The Raman mode at 555.2 cm^{-1} (B$_g$) was assigned as a wagging vibration. The mode centered at 487.0 cm^{-1} (B$_g$)

Table 4 (*continued*)

IR ω_{obs}	IR ω_{cal}	(Sym)	Assignments
	85.3	A_u	Translational mode of the La atoms along of the diagonal of the unit cell and translation of the octahedron along of the axis "c" and in the "ab" plane
	79.3	B_u	Translational mode of the La atoms a long of the "ab" plane plus a wagging of the octahedron with a large motion of the oxygen atoms in the "ab" plane.
	77.1	A_u	Translational mode of the La atoms in the "ac" plane and translation of the octahedron along of the axis "c" and in the "ab" plane

Table 5
Force constants that better fitted the experiment used in the lattice dynamics calculation.

Atomic pair	Force Constant functions (mDyn/Å)
Fe(Mn)–O	$f_{Mn\text{-}O} = 6.07 - 2.1\ r$
La–O	$f_{La\text{-}O} = 1.069 - 0.077\ r$
O–O	$f_{O\text{-}O} = 0.7097 - 0.3663\ r + 0.0503\ r^2$

was assigned to an in-plane scissoring of the octahedrons in the "ab" plane, while the mode located at 472.4 cm^{-1} (B_g) was assigned as an out-of-plane twisting of the octahedrons with motion from the oxygen atoms along the "a" axis. The Raman modes located at 443.2 cm^{-1} (B_g) and 438.8 cm^{-1} were assigned to a bending of the octahedrons, while the mode at 361.9 cm^{-1} (B_g) was assigned to a twisting vibration. The mode at 198.9 cm^{-1} (B_g) was assigned to a translational mode of the La atoms a long of the "c" axis plus a twisting of the octahedrons, while the mode centered at 120 cm^{-1} (B_g) was assigned as a translational mode of the La atoms a long of the "ab" plane plus a twisting of the octahedron. Finally, the mode centered at 77.4 cm^{-1} (B_g) was assigned to a translational mode of the La atoms a long of the "b" axis plus a bending wagging of the octahedrons.

3.2.3. Au infrared modes

The modes located at 740.1 cm^{-1} (A_u) (Figs. 6), 729.9 cm^{-1} (A_u), and 722.5 cm^{-1} (A_u) are assigned as asymmetric stretching (ν_3) of the octahedrons. The modes at 740.1 cm^{-1} (A_u) and 729.9 cm^{-1} (A_u) present a large motion of the oxygen atoms along of the "c" axis and in the

diagonal of the plane "ab", while the mode center at 722.5 cm^{-1} (A_u) is associated with a large motion of the oxygen atoms along of the "ab" plane. The modes calculated at 520.2 cm^{-1} (A_u), 477.1 cm^{-1} (A_u), and 474.1 cm^{-1} (A_u) are assigned as wagging the octahedrons. The modes at 520.2 cm^{-1} (A_u) and 477.1 cm^{-1} (A_u) (Fig. 6) present a large motion of the oxygen atoms along of the diagonal of the unit cell and the mode at 474.1 cm^{-1} (A_u) present a large motion of the oxygen atoms along of the "a" axis. The modes located at 450.2 cm^{-1} (A_u) and 445.5 cm^{-1} (A_u) are assigned as wagging vibration the octahedrons and present respectively a large motion of the oxygen atoms along of the diagonal of the "ac" plane and wagging vibration the octahedrons with a large motion from the oxygen atoms along of the diagonal of the "ab" plane. The next four wagging vibrations of the octahedrons are located at 397.5 cm^{-1} (A_u), 335.8 cm^{-1} (A_u), 315.3 cm^{-1} (A_u), and 291.0 cm^{-1} (A_u). The modes at 397.5 cm^{-1} (A_u) and 291.0 cm^{-1} (A_u) present a large motion of the oxygen atoms along of the diagonal of the unit cell. The mode at 186.8 cm^{-1} (A_u) is a translational mode of the La atoms a long of the "c" axis plus a translational of the octahedron in the "ac" plane and the 120.2 cm^{-1} (A_u) is a translational mode of the La atoms a long of the diagonal of "ac" plane plus a wagging of the octahedrons. The mode located at 95.0 cm^{-1} (A_u) (Fig. 6) is a translational mode of the La atoms and the octahedron along of the axis "b". The mode at 85.3 cm^{-1} (A_u) is a translational mode of the La atoms along of the diagonal of the unit cell and translation of the oxygen atoms of the octahedron along of the "c" axis and in the "ab" plane. Finally, the mode at 77.1 cm^{-1} (A_u) is a translational mode of the La atoms in the "ac" plane and a translation of the oxygen atoms of the octahedron along of the "c" axis and in the "ab" plane.

3.2.4. Bu infrared modes

The modes located at 737.5 cm^{-1} (B_u) (Figs. 6) and 733.4 cm^{-1} (B_u) are asymmetric stretching (ν_3) of the octahedrons with large motion of the oxygen atoms along of the "c" axis and in the diagonal of the plane "ab". The mode at 722.9 cm^{-1} (B_u) is an asymmetric stretching (ν_3) of the octahedrons with large motion of the oxygen atoms along of the diagonal of the plane "ab". The modes located at 564.0 cm^{-1} (B_u) (Figs. 6), 477.1 cm^{-1} (B_u), 464.7 cm^{-1} (B_u), 450.5 cm^{-1} (B_u), 395.4 cm^{-1} (B_u), 330.4 cm^{-1} (B_u), 323.3 cm^{-1} (B_u), and 284.2 cm^{-1} (B_u) are assigned as wagging vibration of the octahedrons and the motion from the oxygen atoms along of the axes, diagonals and planes of the unit cell are described on Table 4. The modes at 133.7 cm^{-1} (B_u), 98.0 cm^{-1} (B_u), 92.7 cm^{-1} (B_u), and 79.3 cm^{-1} (B_u) (Fig. 6) are assigned as combinations
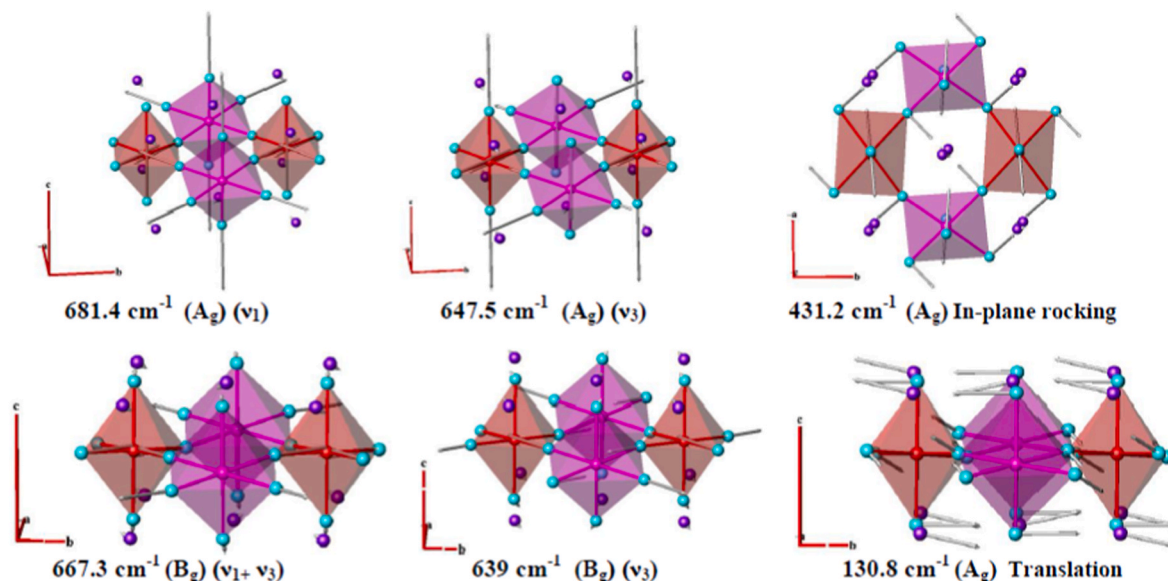

Fig. 5. Calculated wavenumbers and atomic displacements for some Raman modes of the double perovskite La$_2$FeMnO$_6$.

681.4 cm^{-1} (A_g) (ν_1) 647.5 cm^{-1} (A_g) (ν_3) 431.2 cm^{-1} (A_g) In-plane rocking
667.3 cm^{-1} (B_g) ($\nu_1 + \nu_3$) 639 cm^{-1} (B_g) (ν_3) 130.8 cm^{-1} (A_g) Translation

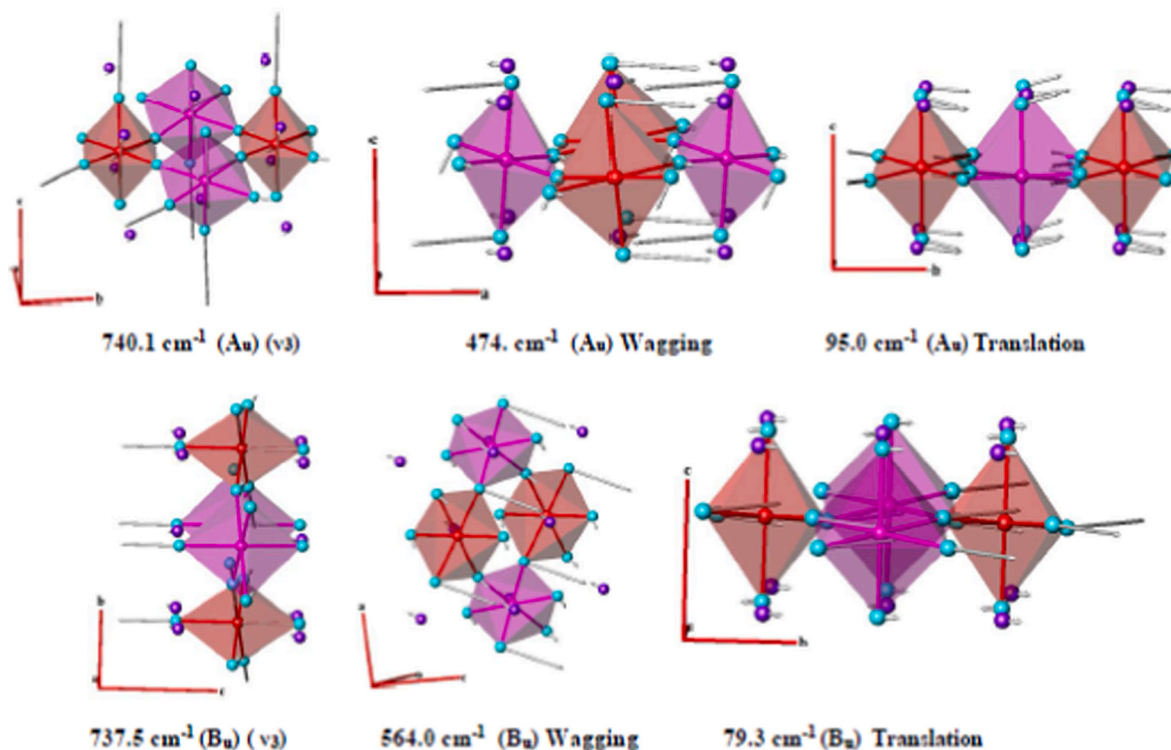**Fig. 6.** Calculated wavenumbers and atomic displacements for some IR modes of the double perovskite La$_2$FeMnO$_6$.

of the translational mode from the La atoms plus a wagging of the octahedron. The details about the motion of the La and O atoms are described on Table 4.

3.3. Mossbauer spectroscopy study

Fig. 7 shows the Mössbauer spectrum for the double perovskite La$_2$FeMnO$_6$ measured at room temperature and its respective fit. The fit showed the presence of two paramagnetic sites, with quadrupole splitting values (Δ) of 1.74 and 0.43 mm/s, which indicate the presence of Fe^{2+} and Fe^{3+} ions, respectively [69]. According to Romero et al. [70], the difference in the oxidation state in iron is due to local distortions caused by the increase in the atomic number of the lanthanide, indicating that the decrease in their radius increases the local distortion

surrounding the iron atom. Besides that, the values of the calculated hyperfine parameters are similar to those found in LaFe$_{(1-x)}$Mn$_x$ double perovskite structures [57,70,71]. Likewise, the absence of ferromagnetic phases at room temperature also corroborates the successful incorporation of iron atoms into the double perovskite matrix.

3.4. Vibrating Sample Magnetometer Study

Fig. 8 shows the magnetization versus applied field (MxH) curve of the double perovskite LFMO performed at room temperature (300 K) in a vibrating sample magnetometer for a maximum applied magnetic field of 13 kOe. The LFMO system provides a complex environment for the
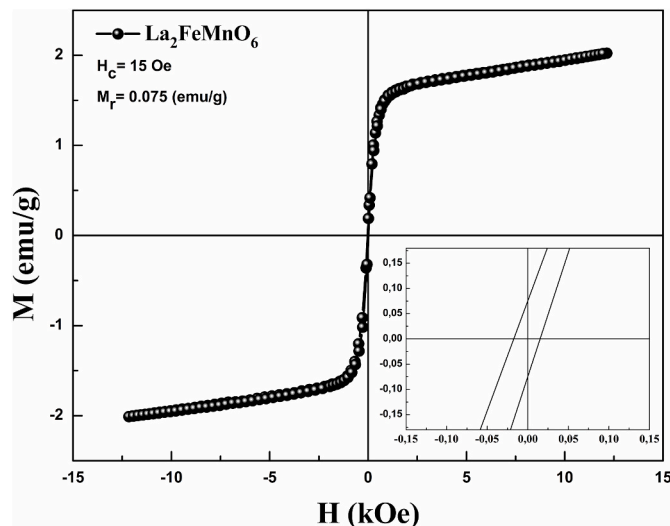

Fig. 7. Mössbauer spectra of the double perovskite La2FeMnO6 measured at room temperature.

Fig. 8. Magnetic hysteresis cycles of the double perovskite La$_2$FeMnO$_6$ performed at room temperature. The inset shows figure enlargement, showing the coercivity value.

competition between ferromagnetic (FM) and antiferromagnetic (AFM) interactions due to the dominant exchange interactions between Mn^{3+} and Fe^{3+} ions. At room temperature, the LFMO hysteresis curve exhibits a weak ferromagnetic (FM) behavior due to the alignment of the Fe^{3+} ions, this is shown in Fig. 6 in mössbauer spectroscopy analyses. Therefore, the analysis of the LFMO hysteresis curve shows a linear behavior for a high magnetic field value and unsaturated curve at a maximum applied field of 12.5 kOe, with a maximum magnetization value of $M_{max} = 2.01$ emu/g. This can be attributed to both the AFM and FM interactions, which require very high-applied magnetic field for saturation. In the work performed by Azevedo Filho et al. [57], uses the RCI technique to obtain nanoparticles of La_2FeMnO_6, it crystallized with the same monoclinic structure with the $P2_1/n$-space group of this work, but there was a big difference in the particle size which is on the order of nanometers. There were no significant differences for the ambient hysteresis curve with the change of method of synthesis and by particle size. The inset in Fig. 8 shows the maximum coercive field obtained from the LFMO sample with a value of $H_c = 15 \pm 1$ Oe. The observed coercivity and retentivity values are due to the presence of ferromagnetic (FM) clusters, which lock-in the magnetic energy after the removal of the applied magnetic field [56]. The LFMO system provides a competition between antiferromagnetic (AFM) and ferromagnetic (FM) interactions, due to exchange interactions between Fe^{3+} and Mn^{3+} ions [57]. The AFM sample signal can be associated with clusters formed by Fe^{3+}-O-Fe^{+3} or Mn^{3+}-O-Mn^{3+}. Meanwhile, the FM signal is associated with the super-exchange interaction between different transition metal ions of the Fe^{3+}-O-Mn^{3+}. The disorder of the system can lead to a decrease in magnetization that possibly happens due to anti-site defects and super exchange interactions between the clusters formed by the AFM signal [55,72]. There is a certain complexity in understanding the magnetic interactions of the LFMO structure system, so further studies on this perovskite double are necessary.

3.5. Electron Paramagnetic Resonance (EPR)

Fig. 9 shows the EPR intensity in the X bands of the La_2FeMnO_6 perovskite duo under different magnetic fields. EPR is widely used in the analysis of the magnetic properties of manganites [73,74] and perovskite doubles [56,75–77]. The LFMO double perovskite EPR spectrum indicates the coexistence of paramagnetic resonance (PM) given by the narrow signal of the curve, and a broad signal corresponding to the antiferromagnetic resonance (AFM), being a strong indication of the coexistence of PM and AFM clusters. The factor g was calculated through the EPR spectra and showed a constant value of the resonant magnetic that corresponds a g-factor of about 1.7657, in agreement with the coexistence of both stated clusters.

4. Conclusions

In summary, the double perovskite (La_2FeMnO_6) compound was synthesized through the solid stated reaction and the XRD pattern of the powder sample was refined to determine the structural parameters. The structural parameters of the La_2FeMnO_6, were identified as monoclinic structure, $P2_1/n$-space group, and with two formulas per unit cell (Z = 2), as well as their lattice parameters are: $a = 5.557$, $b = 5.562$, and $c = 7.873$ Å. The SEM analyses revealed that the sample is formed by particles with quasi-spherical morphology, randomly distributed in clusters. The vibrational properties obtained via experimental Raman and IR spectroscopy of La_2FeMnO_6 were supported with the LD calculation, which was performed by a rigid ion model in order to assign the experimental Raman and IR bands. The investigation by Mössbauer spectroscopy identified that the incorporation of iron atoms occurred successfully in structure La_2FeMnO_6. The magnetization versus applied field (MxH) curve of the double perovskite LFMO was performed at room temperature (300 K) in a vibrating sample magnetometer for a maximum applied magnetic field of 13 kOe. At room temperature, the
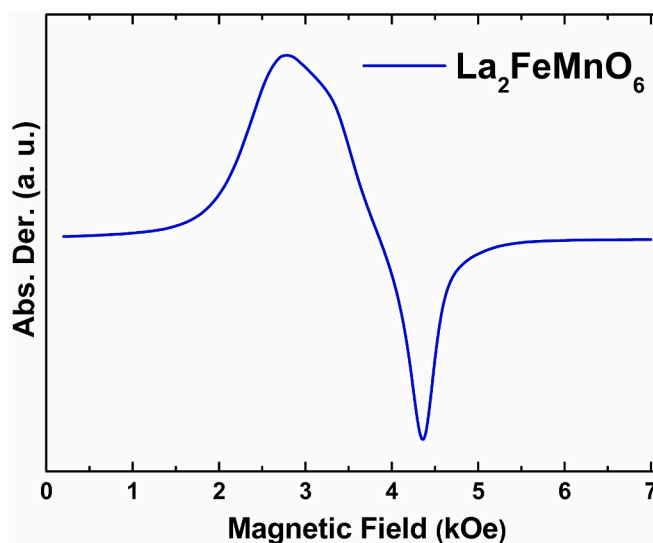

Fig. 9. The X-bands EPR intensity of double perovskite La_2FeMoO_6 under different magnetic fields.

LFMO hysteresis curve exhibited a weak ferromagnetic (FM) behavior due to the alignment of the Fe^{3+} ions. Therefore, the analysis of the LFMO hysteresis curve showed a linear behavior for high magnetic field values, with a maximum magnetization value of $M_{max} = 2.01$ emu/g. The AFM sample signal can be associated with clusters formed by Fe^{3+}-O-Fe^{3+} or Mn^{3+}-O-Mn^{3+}. Meanwhile, the FM signal is associated with the super-exchange interaction between different transition metal ions of the Fe^{3+}-O-Mn^{3+}. The LFMO double perovskite EPR spectrum indicates the coexistence of paramagnetic resonance (PM) and antiferromagnetic resonance (AFM). The basic research of the double perovskite La_2FeMnO_6 related to synthesis and characterization may be found suitable for modern application.

CRediT authorship contribution statement

Raí F. Jucá: Formal analysis, Data curation, Conceptualization. **Gilberto D. Saraiva:** Writing – review & editing, Writing – original draft. **A.J. Ramiro de Castro:** Methodology, Formal analysis. **Francisco F.de Sousa:** Writing – review & editing, Formal analysis, Data curation. **Francisco G.S. Oliveira:** Investigation, Formal analysis, Data curation. **Igor F. Vasconcelos:** Methodology, Formal analysis, Data curation, Conceptualization. **G.D.S. Souza:** Methodology, Formal analysis, Data curation. **João M. Soares:** Methodology, Investigation, Funding acquisition, Conceptualization. **Carlos H.N. Cordeiro:** Methodology, Investigation, Formal analysis, Data curation. **W. Paraguassu:** Writing – review & editing, Software, Methodology, Data curation.

Declaration of competing interest

The authors declare that they have no known competing financial interests or personal relationships that could have appeared to influence the work reported in this paper.

Acknowledgments

References

[1] R. Das, R.N.P. Choudhary, Studies of structural, dielectric relaxation and impedance spectroscopy of lead-free double perovskite: Dy2NiMnO6, J. Mater. Sci. Mater. Electron. 29 (2018) 19099–19110, https://doi.org/10.1007/s10854-018-0036-7.

[2] Y.Q. Lin, X.M. Chen, X.Q. Liu, Relaxor-like dielectric behavior in La2NiMnO6 double perovskite ceramics, Solid State Commun. 149 (2009) 784–787, https://doi.org/10.1016/j.ssc.2009.02.028.

[3] M.H.K. Rubel, T. Takei, N. Kumada, M.M. Ali, A. Miura, K. Tadanaga, K. Oka, M. Azuma, M. Yashima, K. Fujii, E. Magome, C. Moriyoshi, Y. Kuroiwa, J.R. Hester, M. Avdeev, Hydrothermal synthesis, crystal structure, and superconductivity of a double-perovskite Bi oxide, Chem. Mater. 28 (2016) 459–465, https://doi.org/10.1021/acs.chemmater.5b02386.

[4] J. Su, Z.Z. Yang, X.M. Lu, J.T. Zhang, L. Gu, C.J. Lu, Q.C. Li, J.M. Liu, J.S. Zhu, Magnetism-Driven ferroelectricity in double perovskite Y2NiMnO6, ACS Appl. Mater. Interfaces 7 (2015) 13260–13265, https://doi.org/10.1021/acsami.5b00911.

[5] C.S. Kim, S.B. Kim, Crystal Structure and Magnetic Properties of Double Perovskite Sr2 Fe Mo O6, 2001, 10, http://www.npsm-kps.org/journal/view.html.

[6] J.S. Punitha, M. Dhilip, V. Anbarasu, K.S. Kumar, Structural and magnetic properties of Fe, Mn based double perovskite La2FeMnO6 compound, AIP Conf. Proc. 2115 (2019) 6–9, https://doi.org/10.1063/1.5113307.

[7] M. Yarmolich, N. Kalanda, S. Demyanov, J. Fedotova, V. Bayev, N.A. Sobolev, Charge ordering and magnetic properties in nanosized Sr2FeMoO6−δ powders, Phys Status Solidi Basic Res 253 (2016) 2160–2166, https://doi.org/10.1002/pssb.201600527.

[8] L.S. Zaremba, W.H. Smoleński, Optimal portfolio choice under a liability constraint, Ann. Oper. Res. 97 (2000) 131–141, https://doi.org/10.1023/A.

[9] M.K. Wu, S.R. Sheen, D.C. Ling, C.Y. Tai, G.Y. Tseng, D.H. Chen, D.Y. Chen, F. Z. Chien, F.C. Zhang, Superconductivity in a Ru-Based double perovskite, Czechoslov J Phys 46 (1996) 3381–3382, https://doi.org/10.1007/BF02548156.

[10] S.M. Rao, J.K. Srivastava, H.Y Tanga, D.C. Linga, C.C. Chunga, J.L. Yanga, S. R. Sheena, M.K. Wua, Crystal growth of a new superconducting double perovskite A2YRu1−xCuxO6(A=Ba,Sr), J. Cryst. Growth 235 (2002) 271–276.

[11] M. Saiduzzaman, H. Yoshida, T. Takei, S. Yanagida, N. Kumada, M. Nagao, H. Yamane, M. Azuma, M.H.K. Rubel, C. Moriyoshi, Y. Kuroiwa, Hydrothermal synthesis and crystal structure of a (Ba0.54K0.46)4Bi4O12 double-perovskite superconductor with onset of the transition Tc ∼30 K, Inorg. Chem. 58 (2019) 11997–12001, https://doi.org/10.1021/acs.inorgchem.9b01768.

[12] M.H.K. Rubel, A. Miura, T. Takei, N. Kumada, M. Mozahar Ali, M. Nagao, S. Watauchi, I. Tanaka, K. Oka, M. Azuma, E. Magome, C. Moriyoshi, Y. Kuroiwa, A.K.M. Azharul Islam, Superconducting double perovskite bismuth oxide prepared by a low-temperature hydrothermal reaction, Angew. Chem. 126 (2014) 3673–3677, https://doi.org/10.1002/ange.201400607.

[13] W. Zhang, M. Hong, J. Luo, Halide double perovskite ferroelectrics, Angew. Chem. Int. Ed. 59 (2020) 9305–9308, https://doi.org/10.1002/anie.201916254.

[14] W. Guo, X. Liu, S. Han, Y. Liu, Z. Xu, M. Hong, J. Luo, Z. Sun, Room-temperature ferroelectric material composed of a two-dimensional metal halide double perovskite for X-ray detection, Angew. Chem. 132 (2020) 13983–13988, https://doi.org/10.1002/ange.202004235.

[15] S. Yáñez-Vilar, E.D. Mun, V.S. Zapf, B.G. Ueland, J.S. Gardner, J.D. Thompson, J. Singleton, M. Sánchez-Andújar, J. Mira, N. Biskup, M.A. Señarís-Rodríguez, C. D. Batista, Multiferroic behavior in the double-perovskite Lu2MnCoO 6, Phys Rev B - Condens Matter Mater Phys. 84 (2011) 1–8, https://doi.org/10.1103/PhysRevB.84.134427.

[16] R. Nechache, C.V. Cojocaru, C. Harnagea, C. Nauenheim, M. Nicklaus, A. Ruediger, F. Rosei, A. Pignolet, Epitaxial patterning of Bi2FeCrO6 double perovskite nanostructures: multiferroic at room temperature, Adv. Mater. 23 (2011) 1724–1729, https://doi.org/10.1002/adma.201004405.

[17] Y. Shimakawa, M. Azuma, N. Ichikawa, Multiferroic compounds with double-perovskite structures, Materials 4 (2010) 153–168, https://doi.org/10.3390/ma4010153.

[18] T. Goto, T. Kimura, G. Lawes, A.P. Ramirez, Y. Tokura, Ferroelectricity and giant magnetocapacitance in perovskite rare-earth manganites, Phys. Rev. Lett. 92 (2004) 1–4, https://doi.org/10.1103/PhysRevLett.92.257201.

[19] T. Kimura, T. Goto, H. Shintani, K. Ishizaka, T. Arima, Y. Tokura, Magnetic control of ferroelectric polarization, Nature 426 (2003) 55–58, https://doi.org/10.1038/nature02018.

[20] S.W. Cheong, M. Mostovoy, Multiferroics: a magnetic twist for ferroelectricity, Nat. Mater. 6 (2007) 13–20, https://doi.org/10.1038/nmat1804.

[21] T. Kimura, Spiral magnets as magnetoelectrics, Annu. Rev. Mater. Res. 37 (2007) 387–413, https://doi.org/10.1146/annurev.matsci.37.052506.084259.

[22] T.H. Arima, Ferroelectricity induced by proper-screw type magnetic order, J Phys Soc Japan 76 (2007) 1–4, https://doi.org/10.1143/JPSJ.76.073702.

[23] M. Kenzelmann, G. Lawes, A.B. Harris, G. Gasparovic, C. Broholm, A.P. Ramirez, G. A. Jorge, M. Jaime, S. Park, Q. Huang, A.Y. Shapiro, L.A. Demianets, Direct transition from a disordered to a multiferroic phase on a triangular lattice, Phys. Rev. Lett. 98 (2007) 2–5, https://doi.org/10.1103/PhysRevLett.98.267205.

[24] H. Katsura, N. Nagaosa, A.V. Balatsky, Spin current and magnetoelectric effect in noncollinear magnets, Phys. Rev. Lett. 95 (2005) 1–4, https://doi.org/10.1103/PhysRevLett.95.057205.

[25] G. Lawes, A.B. Harris, T. Kimura, N. Rogado, R.J. Cava, A. Aharony, O. Entin-Wohlman, T. Yildirim, M. Kenzelmann, C. Broholm, A.P. Ramirez, Magnetically driven ferroelectric order in Ni3V2O8, Phys. Rev. Lett. 95 (2005) 1–4, https://doi.org/10.1103/PhysRevLett.95.087205.

[26] N. Hur, S. Park, P.A. Sharma, J.S. Ahn, S. Guha, S.W. Cheong, Electric polarization reversal and memory in a multiferroic material induced by magnetic fields, Nature 429 (2004) 392–395, https://doi.org/10.1038/nature02572.

[27] M.C. Viola, M.J. Martínez-Lope, J.A. Alonso, P. Velasco, J.L. Martínez, J. C. Pedregosa, R.E. Carbonio, M.T. Fernández-Díaz, Induction of colossal magnetoresistance in the double perovskite Sr2CoMoO6, Chem. Mater. 14 (2002) 812–818, https://doi.org/10.1021/cm011186j.

[28] R.N. Mahato, K. Sethupathi, V. Sankaranarayanan, Colossal magnetoresistance in the double perovskite oxide La2CoMnO6, J. Appl. Phys. 107 (2010) 4–7, https://doi.org/10.1063/1.3350907.

[29] S. Ray, S. Middey, S. Jana, A. Banerjee, P. Sanyal, R. Rawat, L. Gregoratti, D. D. Sarma, Origin of the unconventional magnetoresistance in Sr2FeMoO6, Epl 94 (2011), https://doi.org/10.1209/0295-5075/94/47007.

[30] N.A. Kalanda, S.E. Demyanov, A.V. Petrov, D.V. Karpinsky, M.V. Yarmolich, S. K. Oh, S.C. Yu, D.H. Kim, Interrelation between the structural, magnetic and magnetoresistive properties of double-perovskite Sr2FeMoO6−δ thin films, J. Electron. Mater. 45 (2016) 3466–3472, https://doi.org/10.1007/s11664-016-4478-5.

[31] Y. Mao, J. Parsons, J.S. McCloy, Magnetic properties of double perovskite La2BMnO6 (B = Ni or Co) nanoparticles, Nanoscale 5 (2013) 4720–4728, https://doi.org/10.1039/c3nr00825h.

[32] M. Hashisaka, D. Kan, A. Masuno, M. Takano, Y. Shimakawa, T. Terashima, K. Mibu, Epitaxial growth of ferromagnetic La2NiMnO6 with ordered double-perovskite structure, Appl. Phys. Lett. 89 (2006), https://doi.org/10.1063/1.2226997.

[33] N.S. Rogado, J. Li, A.W. Sleight, M.A. Subramanian, Magnetocapacitance and magnetoresistance near room temperature in a ferromagnetic semiconductor: La2NiMnO6, Adv. Mater. 17 (2005) 2225–2227, https://doi.org/10.1002/adma.200500737.

[34] P. Padhan, H.Z. Guo, P. Leclair, A. Gupta, Dielectric relaxation and magnetodielectric response in epitaxial thin films of La2NiMnO6, Appl. Phys. Lett. 92 (2008), https://doi.org/10.1063/1.2832642.

[35] M.N. Iliev, H. Guo, A. Gupta, Raman spectroscopy evidence of strong spin-phonon coupling in epitaxial thin films of the double perovskite La2NiMnO6, Appl. Phys. Lett. 90 (2007) 88–91, https://doi.org/10.1063/1.2721142.

[36] H. Guo, J. Burgess, S. Street, A. Gupta, T.G. Calvarese, M.A. Subramanian, Growth of epitaxial thin films of the ordered double perovskite La2NiMnO6 on different substrates, Appl. Phys. Lett. 89 (2006), https://doi.org/10.1063/1.2221894, 0–3.

[37] J. Luo, S. Li, H. Wu, Y. Zhou, Y. Li, J. Liu, J. Li, K. Li, F. Yi, G. Niu, J. Tang, Cs2AgInCl6 double perovskite single crystals: parity forbidden transitions and their application for sensitive and fast UV photodetectors, ACS Photonics 5 (2018) 398–405, https://doi.org/10.1021/acsphotonics.7b00837.

[38] Z. Lu, Y. Meng, L. Wen, M. Huang, L. Zhou, L. Liao, D. He, Double perovskite Ba2LaNbO6:Mn4+,Yb3+ phosphors: potential application to plant-cultivation LEDs, Dyes Pigments 160 (2019) 395–402, https://doi.org/10.1016/j.dyepig.2018.08.023.

[39] X. Geng, Y. Xie, Y. Ma, Y. Liu, J. Luo, J. Wang, R. Yu, B. Deng, W. Zhou, Abnormal thermal quenching and application for w-LEDs: double perovskite Ca2InSbO6:Eu3+ red-emitting phosphor, J. Alloys Compd. 847 (2020), 156249, https://doi.org/10.1016/j.jallcom.2020.156249.

[40] G. Jiang, B. Yang, G. Zhao, Y. Liu, J. Zou, H. Sun, H. Ou, Y. Fang, J. Hou, High quantum efficiency far red emission from double perovskite structured CaLaMgMO6:Mn4+ (M = Nb, Ta) phosphor for UV-based light emitting diodes application, Opt Mater (Amst). 83 (2018) 93–98, https://doi.org/10.1016/j.optmat.2018.05.074.

[41] W. Ran, H.M. Noh, S.H. Park, B.R. Lee, J.H. Kim, J.H. Jeong, J. Shi, G. Liu, Simultaneous bifunctional application of solid-state lighting and ratiometric optical thermometer based on double perovskite LiLaMgWO6:Er3+ thermochromic phosphors, RSC Adv. 9 (2019) 7189–7195, https://doi.org/10.1039/c8ra10242b.

[42] M. Sariful Sheikh, D. Ghosh, A. Dutta, S. Bhattacharyya, T.P. Sinha, Lead free double perovskite oxides Ln2NiMnO6 (Ln = La, Eu, Dy, Lu), a new promising material for photovoltaic application, Mater Sci Eng B Solid-State Mater Adv Technol. 226 (2017) 10–17, https://doi.org/10.1016/j.mseb.2017.08.027.

[43] M.S. Shadabroo, H. Abdizadeh, M.R. Golobostanfard, Elpasolite structures based on A2AgBiX6 (A: MA, Cs, X: I, Br): application in double perovskite solar cells, Mater. Sci. Semicond. Process. 125 (2021), https://doi.org/10.1016/j.mssp.2020.105639.

[44] C. Tablero, Photovoltaic application of the multiferroic Bi2FeCrO6 double perovskite, Sol. Energy 137 (2016) 173–178, https://doi.org/10.1016/j.solener.2016.08.004.

[45] B. Zhao, L. Zhang, D. Zhen, S. Yoo, Y. Ding, D. Chen, Y. Chen, Q. Zhang, B. Doyle, X. Xiong, M. Liu, A tailored double perovskite nanofiber catalyst enables ultrafast oxygen evolution, Nat. Commun. 8 (2017) 1–9, https://doi.org/10.1038/ncomms14586.

[46] A. Grimaud, K.J. May, C.E. Carlton, Y.L. Lee, M. Risch, W.T. Hong, J. Zhou, Y. Shao-Horn, Double perovskites as a family of highly active catalysts for oxygen evolution in alkaline solution, Nat. Commun. 4 (2013) 1–7, https://doi.org/10.1038/ncomms3439.

[47] L. Zhou, Y.F. Xu, B.X. Chen, D. Bin Kuang, C.Y. Su, Synthesis and photocatalytic application of stable lead-free Cs2AgBiBr6 perovskite nanocrystals, Small 14 (2018) 1–7, https://doi.org/10.1002/smll.201703762.

[48] Z. Liu, H. Yang, J. Wang, Y. Yuan, K. Hills-Kimball, T. Cai, P. Wang, A. Tang, O. Chen, Synthesis of lead-free Cs2AgBix6 (X = Cl, Br, I) double perovskite nanoplatelets and their application in CO2 photocatalytic reduction, Nano Lett. 21 (2021) 1620–1627, https://doi.org/10.1021/acs.nanolett.0c04148.

[49] Z. Meng, J. Xu, P. Yu, X. Hu, Y. Wu, Q. Zhang, Y. Li, L. Qiao, Y. Zeng, H. Tian, Double perovskite La_2CoMnO_6 hollow spheres prepared by template impregnation for high-performance supercapacitors, Chem. Eng. J. 400 (2020), 125966, https://doi.org/10.1016/j.cej.2020.125966.

[50] R. Ramesh, N.A. Spaldin, Multiferroics: progress and prospects in thin films, Nanosci Technol A Collect Rev from Nat Journals 3 (2009) 20–28, https://doi.org/10.1142/9789814287005_0003.

[51] K. Jiang, J.J. Zhu, J.D. Wu, J. Sun, Z.G. Hu, J.H. Chu, Influences of oxygen pressure on optical properties and interband electronic transitions in multiferroic bismuth ferrite nanocrystalline films grown by pulsed laser deposition, ACS Appl. Mater. Interfaces 3 (2011) 4844–4852, https://doi.org/10.1021/am201340d.

[52] W. Eerenstein, N.D. Mathur, J.F. Scott, Multiferroic and magnetoelectric materials, Nature 442 (2006) 759–765, https://doi.org/10.1038/nature05023.

[53] X. Wang, K. Li, H. Xu, N. Ali, Y. Wang, Q. Shen, H. Wu, Synthesis of large two-dimensional lead-free bismuth-silver double perovskite microplatelets and their application for field-effect transistors, Chem. Commun. 56 (2020) 7917–7920, https://doi.org/10.1039/d0cc01847c.

[54] D. Triyono Yunida, The influence of calcination temperature on the structural properties of La_2FeMnO_6 double perovskite materials, IOP Conf. Ser. Mater. Sci. Eng. 902 (2020), https://doi.org/10.1088/1757-899X/902/1/012027.

[55] M. Dhilip, N.A. Devi, J.S. Punitha, V. Anbarasu, K.S. Kumar, Conventional synthesis and characterization of cubically ordered La_2FeMnO_6 double perovskite compound, Vacuum 167 (2019) 16–20, https://doi.org/10.1016/j.vacuum.2019.05.028.

[56] J. Pezhumkattil Palakkal, P.N. Lekshmi, S. Thomas, K.G. Suresh, M.R. Varma, Observation of high-temperature magnetic transition and existence of ferromagnetic short-range correlations above transition in double perovskite La_2FeMnO_6, RSC Adv. 5 (2015), https://doi.org/10.1039/c5ra24092a, 105531–105536.

[57] J.B. de Azevedo Filho, J.H. de Araújo, M.A. Morales, C.L. Firme, J.B. de Oliveira, Exchange bias and spin glass in La_2FeMnO_6 nanoparticles, J. Magn. Magn Mater. 471 (2019) 177–184, https://doi.org/10.1016/j.jmmm.2018.09.093.

[58] P. Barrozo, N.O. Moreno, J.A. Aguiar, Ferromagnetic cluster on La2FeMnO6, Adv. Mater. Res. 975 (2014) 122–127. https://doi.org/10.4028/www.scientific.net/AMR.975.122.

[59] D. Yang, T. Yang, P. Mukherjee, S.E. Dutton, D. Huo, M.A. Carpenter, Strain coupling and acoustic attenuation associated with glassy magnetic phase transitions in the disordered double perovskite La_2FeMnO_6, Phys. Rev. B 99 (2019) 1–12, https://doi.org/10.1103/PhysRevB.99.094314.

[60] A. Raj, M. Kumar, D. Mishra, A. Anshul, Raman and photoluminescence spectral studies in epitaxial Bi_2NiMnO_6 double perovskite thin-film samples, Opt Mater (Amst). 101 (2020), 109773, https://doi.org/10.1016/j.optmat.2020.109773.

[61] A. Ezzahi, B. Manoun, A. Ider, L. Bih, S. Benmokhtar, M. Azrour, M. Azdouz, J. M. Igartua, P. Lazor, X-ray diffraction and Raman spectroscopy studies of $BaSrMWO_6$ (MNi, Co, Mg) double perovskite oxides, J. Mol. Struct. 985 (2011) 339–345, https://doi.org/10.1016/j.molstruc.2010.11.017.

[62] X. Luo, L. Bai, J. Xing, X. Zhu, D. Xu, B. Xie, Z. Gan, G. Li, H. Liang, Ordered mesoporous cobalt containing perovskite as a high-performance heterogeneous catalyst in activation of peroxymonosulfate, ACS Appl. Mater. Interfaces 11 (2019) 35720–35728, https://doi.org/10.1021/acsami.9b11322.

[63] R.X. Silva, R.L. Moreira, R.M. Almeida, R. Paniago, C.W.A. Paschoal, Intrinsic dielectric properties of magnetodielectric La_2CoMnO_6, J. Appl. Phys. 117 (2015) 1–8, https://doi.org/10.1063/1.4921441.

[64] M. Nasir, M. Khan, S.A. Agbo, S. Bhatt, S. Kumar, S. Sen, Evidence of cluster-glass and Griffiths-like phases in partially ordered La_2FeMnO_6 double perovskite, J. Phys. D Appl. Phys. 53 (2020), https://doi.org/10.1088/1361-6463/ab9263.

[65] E. Dowty, Vibrational interactions of tetrahedra in silicate glasses and crystals - I. calculations on ideal silicate-aluminate-germanate structural units, Phys. Chem. Miner. 14 (1987) 80–93, https://doi.org/10.1007/BF00311151.

[66] G.D. Saraiva, W. Paraguassu, M. MacZka, P.T.C. Freire, F.F. De Sousa, J. Mendes Filho, Temperature-dependent Raman scattering studies on $Na_2Mo_2O_7$ disodium dimolybdate, J. Raman Spectrosc. 42 (2011) 1114–1119, https://doi.org/10.1002/jrs.2836.

[67] M. MacZka, M. Ptak, C. Luz-Lima, P.T.C. Freire, W. Paraguassu, S. Guerini, J. Hanuza, Pressure-induced phase transitions in multiferroic $RbFe(MoO_4)_2$ - Raman scattering study, J. Solid State Chem. 184 (2011) 2812–2817, https://doi.org/10.1016/j.jssc.2011.08.032.

[68] M. Maczka, W. Paraguassu, P.T.C. Freire, A.G. Souza Filho, J. Mendes Filho, J. Hanuza, Lattice dynamics and pressure-induced phase transitions in $Bi_2W_2O_9$: high-pressure Raman study, Phys. Rev. B 81 (2010), 104301, https://doi.org/10.1103/PhysRevB.81.104301.

[69] M.D. Dyar, D.G. Agresti, M.W. Schaefer, C.A. Grant, E.C. Sklute, Mössbauer spectroscopy of Earth and planetary materials, Annu. Rev. Earth Planet Sci. 34 (2006) 83–125, https://doi.org/10.1146/annurev.earth.34.031405.125049.

[70] M. Romero, R. Faccio, J. Martínez, H. Pardo, B. Montenegro, C.C. Plá Cid, A. A. Pasa, Á.W. Mombrú, Effect of lanthanide on the microstructure and structure of $LnMn_{0.5}Fe_{0.5}O_3$ nanoparticles with Ln=La, Pr, Nd, Sm and Gd prepared by the polymer precursor method, J. Solid State Chem. 221 (2015) 325–333, https://doi.org/10.1016/j.jssc.2014.10.028.

[71] V.D. Sedykh, V.S. Shekhtman, A.V. Dubovitskiĭ, I.I. Zver'Kova, V.I. Kulakov, Mössbauer and X-Ray studies of the dynamics of phase transformations and suppression of polymorphism in the $LaMn_{1-x}Fe_xO_{3+\delta}$ compound (x = 0.015-0.500), Phys. Solid State 51 (2009) 373–380, https://doi.org/10.1134/S1063783409020280.

[72] Z.X. Wei, Y. Wang, J.P. Liu, C.M. Xiao, W.W. Zeng, Synthesis, magnetization and photocatalytic activity of $LaFeO_3$ and $LaFe_{0.5}Mn_{0.5}O_{3-\delta}$, Mater. Chem. Phys. 136 (2012) 755–761, https://doi.org/10.1016/j.matchemphys.2012.07.052.

[73] X.J. Liu, Z.Q. Li, A. Yu, M.L. Liu, W.R. Li, B.L. Li, P. Wu, H.L. Bai, E.Y. Jiang, Magnetic, electrical transport and electron spin resonance studies of Fe-doped manganite $LaMn_{0.7}Fe_{0.3}O_{3+\delta}$, J. Magn. Magn Mater. 313 (2007) 354–360, https://doi.org/10.1016/j.jmmm.2007.02.003.

[74] J. Deisenhofer, D. Braak, H.A. Krug Von Nidda, J. Hemberger, R.M. Eremina, V. A. Ivanshin, A.M. Balbashov, G. Jug, A. Loidl, T. Kimura, Y. Tokura, Observation of a griffiths phase in paramagnetic $La_{1-x}Sr_xMnO_3$, Phys. Rev. Lett. 95 (2005) 2–5, https://doi.org/10.1103/PhysRevLett.95.257202.

[75] R.A. Eichel, Structural and dynamic properties of oxygen vacancies in perovskite oxides - analysis of defect chemistry by modern multi-frequency and pulsed EPR techniques, Phys. Chem. Chem. Phys. 13 (2011) 368–384, https://doi.org/10.1039/b918782k.

[76] A. Karmakar, M.S. Dodd, S. Agnihotri, E. Ravera, V.K. Michaelis, Cu(II)-Doped $Cs_2SbAgCl_6$ double perovskite: a lead-free, low-bandgap material, Chem. Mater. 30 (2018) 8280–8290, https://doi.org/10.1021/acs.chemmater.8b03755.

[77] L. Ortega-San Martin, J.P. Chapman, L. Lezama, J. Sánchez Marcos, J. Rodríguez-Fernández, M.I. Arriortua, T. Rojo, Magnetic properties of the ordered double perovskite Sr_2MnTeO_6, Eur. J. Inorg. Chem. (2006) 1362–1370, https://doi.org/10.1002/ejic.200500880.